A strong, lightweight, and damping cermet material with a nacre-like ultrafine 3D interpenetrated architecture

Yanyan Liu [1,2], Xi Xie [1], Zengqian Liu [1,2,*], Qin Yu [3], Qing Jia [1,2], Shaogang Wang [1], Zhefeng Zhang [1,2,*], Rui Yang [1,4,*], Robert O. Ritchie [3,*]

[1] Institute of Metal Research, Chinese Academy of Sciences, Shenyang 110016, China
[2] School of Materials Science and Engineering, University of Science and Technology of China, Hefei 230026, China
[3] Department of Materials Science and Engineering, University of California Berkeley, Berkeley CA 94720, USA
[4] Center for Adaptive System Engineering, School of Creativity and Art, ShanghaiTech University, Shanghai 201210, China

While materials that are light, strong, tough and simultaneously damping are highly attractive for a range of applications, it remains a challenge to achieve a combination of all these properties in a single material as these properties are often mutually exclusive. Here we present a cermet material comprising an ultrafine-grained Mg-Al-Zn magnesium alloy with ultrafine Ti_3AlC_2 ceramic platelets, where the two phases are bi-continuous and interpenetrated in 3D space yet are alternately arranged in a layered fashion as in natural nacre. Such an architecture was constructed by infiltrating the alloy into the porous ceramic scaffold where the Ti_3AlC_2 platelets were preferentially aligned by vacuum filtration and partially sintered. The resulting cermet exhibits a high flexural strength exceeding 1 GPa and a high specific flexural strength (strength normalized by density) of over 350 MPa/(g cm^{-3}) – both exceeding those of most other bulk magnesium (and magnesium alloys), ceramics, and their composite materials – as well as high damping capacities and good fracture toughness. The architectural design strategy and the robust fabrication approach may prove to be effective for developing new high-performance cermet materials.

Keywords: Cermet material; Strength; Damping capacity; Nacre-like composite; 3D interpenetrated architecture

Introduction

There is an omnipresent need to develop new structural materials that are strong yet lightweight, *i.e.*, with a high strength-to-density ratio, but which additionally are resistant to fracture, *i.e.*, less sensitive to flaws, to ensure a safe service life. Damping capacity can also be a key property as it is critical to reduce vibrations and noise while maintaining structural stability. Unfortunately, the major challenge to creating materials that exhibit all these characteristics, namely high specific strength, toughness and damping capacity, is that these properties are generally mutually exclusive, the tradeoffs between strength and toughness [1,2] and between strength and damping capacity [3,4] being well-known examples. However, the question that we pose here is whether this can be overcome by combining different classes of materials.

Ceramics and metals are two of the most common categories of materials in engineering applications. Ceramics generally display high melting temperatures, high modulus, high hardness and good thermal stability owing to their strong covalent (and sometimes ionic) atomic bonding; however, the resulting limited atomic mobility and dislocation activity invariably result in poor fracture toughness, low damping capacity, along with high flaw sensitivity. As such, ceramics tend to exhibit far inferior strength

* Corresponding authors.
E-mail addresses: Liu, Z. (zengqianliu@imr.ac.cn), Zhang, Z. (zhfzhang@imr.ac.cn), Yang, R. (yangrui@shanghaitech.edu.cn), Ritchie, R.O. (roritchie@lbl.gov).

1369-7021/© 2022 Elsevier Ltd. All rights reserved. https://doi.org/10.1016/j.mattod.2022.12.002

where tensile stresses are present, compared to their mechanical performance in compression [5,6]. By comparison, metals generally have much superior ductility, fracture toughness and damping capacity owing to their more compliant metallic bonding. Magnesium and magnesium alloys are particularly attractive in this regard as they have low density and high specific strengths and damping capacity that exceed the majority of other metals [7,8]. However, they display relatively low strengths, stiffness and hardness (in terms of the absolute values) especially at elevated temperatures, which limits their range of application.

A feasible approach to combine the property advantages of ceramics ("cer") and metals ("met") is to make hybrid or composite materials consisting of these two constituents; these have been termed "cermets" [9–13]. The properties of cermet materials are mainly determined by two factors, *i.e.*, the types of components and the composite architectures. Accordingly, the exploitation of high-performance magnesium-ceramic cermet materials principally involves: i) the selection of a ceramic component that has attractive properties yet strongly bonds with magnesium, and ii) the modulation of their architectural (or structural) characteristics, including spatial arrangement, dimensions and orientation of the components. In general, cermet materials have been developed in terms of a structure where ceramic particles acting as a reinforcement phase are dispersed, but are not continuous, within a continuous metal matrix [10–12]. This is represented, for example, by the well-known tungsten carbide-cobalt composites widely used in cutting tools where cobalt plays a role as a binder to bond tungsten carbide particles together [13]. However, it is not easy to construct and process complex architectures, *e.g.*, with special orientations, in cermet materials while ensuring the continuity and fine dimensions of both the ceramic and metal components; indeed, these limitations have served to curtail the extent to which the property advantages of the two phases can be realized. For magnesium-ceramic systems (in bulk form) [14–22], the flexural strength has never reached 1 GPa with a specific flexural strength less than 200 MPa/(g cm^{-3}).

Here we propose a strategy for developing new lightweight, strong and damping magnesium-ceramic cermet materials. First, a Ti_3AlC_2 ceramic was selected as one constituent; this is one of the known MAX phases where a mixed metallic-covalent-ionic atomic bonding state exists [23,24]. MAX phases exhibit a high modulus, hardness and thermal stability like ceramics, yet can conduct heat and electricity like metals, and to some extent are resistant to crack propagation owing to their layered structure [25,26]. In particular, the Ti_3AlC_2 ceramic has been reported to have a high damping capacity among ceramic materials and display a strong interfacial bonding with magnesium [14,23,27]. Second, ultrafine ceramic platelets, obtained by controlled ball-milling, were preferentially aligned by vacuum filtration, and then partially sintered to create interconnections between them, forming an open porous scaffold. Subsequent infiltration of the scaffold with a magnesium melt led to the formation of a cermet material where the metal and ceramic phases are bi-continuous, interpenetrated in 3D space, and alternately arranged in a layered fashion (akin to natural nacre [28–30]). Third, the growth of magnesium grains was constrained within the narrow interspaces between ceramic platelets during the solidification process after infiltration, endowing the magnesium phase with an ultrafine-grained structure. This, along with the ultrafine dimensions of ceramic platelets, further resulted in a high density of interfaces in the composite. Based on these compositional and architectural designs, the resultant cermet material achieved a remarkable combination of properties, including a high flexural strength over 1 GPa and a high specific flexural strength over 350 MPa/(g cm^{-3}), both exceeding those of most other bulk metals, ceramics and their composites, along with good toughness and damping capacity.

Results

As shown in Fig. 1(a), the ceramic platelets are partially interconnected between each other and are interpenetrated with the continuous metal phase in the cermet material. Their width and thickness are in a range of 0.2 to 2 μm and 100 to 300 nm, respectively. The existence of interconnections between the ceramic platelets can be seen in the micrographs of the ceramic scaffold before infiltration and can be verified by the good integrity of the scaffolds shown by their high compressive strength of ~30 MPa, as shown in Fig. S1 in the Supplementary Materials. These platelets are preferentially aligned along the horizontal direction, *i.e.*, normal to the thickness of the composite material, and are alternately arranged with the metal phase filling the interspace between them. Such an architecture is qualitatively similar to the well-known "brick-and-mortar" structure of natural nacre in abalone shells, although not as regular or well organized [28]. However, the ceramic platelets and metal phase in our composite play the respective roles of the "bricks" and the "mortar", as in nacre. Indeed, the mineral bricks in nacre are also interconnected through mineral bridges and are interpenetrated with an organic mortar [29].

The volume fraction of the ceramic phase in the cermet material was determined to be ~44.2 vol.% by analyzing transmission electron microscopy (TEM) images. This is consistent with the measured porosity of the ceramic scaffold before infiltration as ~54.1 vol.% (*i.e.*, corresponding to a ceramic content of ~45.9 vol.%). Only a limited number of tiny pores with an equivalent diameter smaller than 7 μm were detected (in a volume of ~3.1×10^7 μm^3) in the cermet material, as shown in the X-ray tomography (XRT) images in Fig. S2. These pores have a negligible volume fraction (determined by XRT to be ~2×10^{-4} vol.%), indicating a nearly complete filling of the ceramic scaffold with magnesium alloy by melt infiltration. The metal phase has an ultrafine-grained structure typically with a grain size smaller than 1 μm, despite the slow solidification process after melt infiltration (Fig. 1(b)). This results from the constraint on the growth of the metal grains by the ceramic platelets within their interspaces. Additionally, micro defects, such as cracks between the atomic layers, are easily introduced into the ceramic platelets by kinking or delamination during mechanical ball milling due to the relatively weak inter-layer bonding of the layered structure [31,32]. These defects can be largely eliminated during the melt infiltration process and thereby prevented from being inherited in the cermet material. Two possible means to achieve this are to fill the cracks with the metal phase and/or to separate the platelets into smaller ones at the defects, as shown in Fig. 1(c) and Fig. S3.

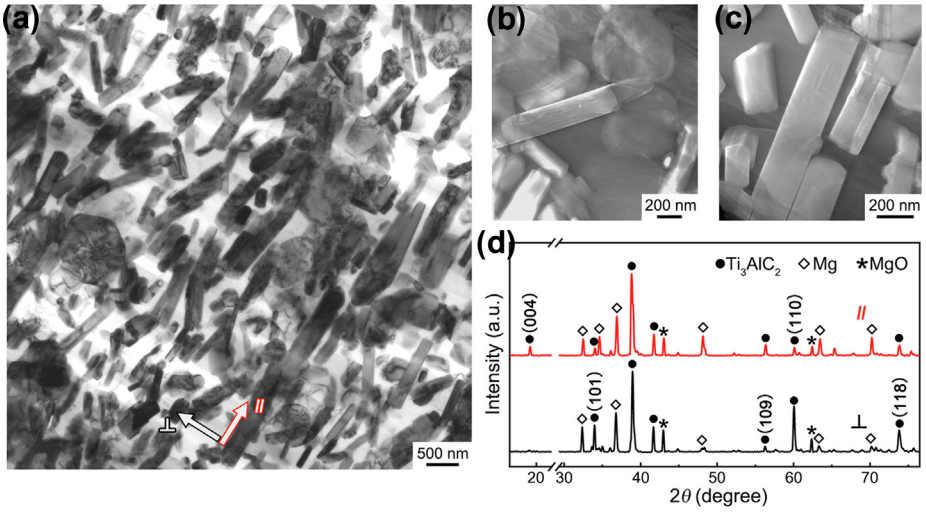

FIGURE 1

Microstructure and phase constitution of the cermet material. (a) TEM micrograph of the through-thickness section of the cermet material showing the ultrafine 3D interpenetrated architecture with the ceramic platelets preferentially aligned and alternately arranged with the metal phase as in natural nacre. (b, c) Scanning TEM micrographs showing (b) the ultrafine-grained structure of the metal phase and (c) the separation of ceramic platelet into smaller ones in the composite. (d) XRD patterns of the cermet material on the horizontal (||) and vertical (⊥) sections which are respectively perpendicular and parallel to its thickness direction.

X-ray diffraction (XRD) results indicated that the cermet material is mainly composed of Ti_3AlC_2 and Mg phases (Fig. 1 (d)), although a small amount of MgO can be detected from the reaction of magnesium with the surface oxides of the ceramic platelets during the melt infiltration process. These oxides, which were determined to be alumina [32], are formed during the ball milling of the ceramic powders to ultrafine dimensions (the oxygen contents in the ceramic powders before and after ball milling were respectively measured to be ~0.75 wt.% and ~4.2 wt.%). The diffraction peaks of the Ti_3AlC_2 phase showed a marked difference in their relative intensities for the horizontal and vertical sections of the cermet material, which are respectively perpendicular and parallel to its thickness direction, indicating a clear anisotropy of architecture. Specifically, the (004) peak appears stronger on the horizontal plane than on the vertical one, which is opposite for the (110) peak, conforming well to the preferential alignment of the ceramic platelets.

The anisotropic architecture of the cermet material leads to an apparent difference in mechanical properties along different directions. As shown in Fig. 2(a), the material exhibits a high compressive strength up to 1006 ± 14 MPa in the horizontal direction at room temperature, but with only limited plastic deformation prior to fracture. In comparison, in the vertical direction the compressive strength is lower at 779 ± 13 MPa, but accompanied by an improvement in plasticity. Thermal analysis results indicated that significant oxidation, as manifested by

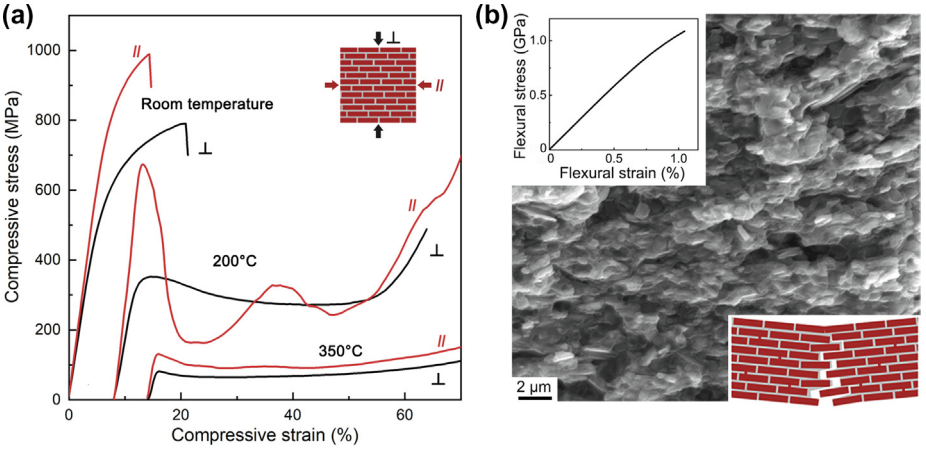

FIGURE 2

Compressive and flexural properties of the cermet material. (a) Representative engineering compressive stress–strain curves of the cermet material, loaded along the horizontal (||) and vertical (⊥) directions and measured at room temperature and elevated temperatures of 200 °C and 350 °C. The inset illustrates the loading configurations with respect to its architecture. (b) SEM micrograph of the fracture surface of the cermet material after bending. The insets show the representative flexural stress–strain curve (upper) and fracture mechanisms (lower) of the material.

the weight increase or an exothermic event, does not occur in the cermet material in air until heating above ~560 °C, *i.e.*, ~36 °C lower than the melting point of the Mg-Al-Zn AZ91D Mg-alloy (Fig. S4). At 200 °C, the compressive stress in the cermet material reaches a peak value of 693 ± 22 MPa along the horizontal direction, followed by a decrease to ~160–300 MPa, before progressively increasing again once the compressive strain exceeds ~40%. Along the vertical direction, the material exhibits a smaller peak stress of 321 ± 29 MPa, and then displays a relatively stable stress plateau at ~200–270 MPa – this is a typical feature observed in cellular materials for energy absorption [4,33]) – until the final increase of stress at a strain above ~50%. With an increase in temperature to 350 °C, the stress plateau behavior appears more stable (with a strain over 60% needed for the final stress increase), but the plateau stresses are reduced to ~100 MPa and ~70 MPa respectively along the horizontal and vertical directions. Unlike the catastrophic fracture at room temperature, more uniform deformation was seen over the entire material at elevated temperatures, leading to gradual compressive flattening of the sample without complete rupture (Fig. S5). In contrast, monolithic magnesium and magnesium alloys generally exhibit much lower strengths at elevated temperatures [34,35], *e.g.*, with (0.2% offset) compressive yield strengths for the AZ91D Mg-alloy respectively on the order of ~54 MPa at 200 °C and ~28 MPa at 350 °C (Fig. S6).

The flexural strength of the cermet material also reaches 1 GPa (1002 ± 68 MPa) at room temperature when loaded along the vertical direction, *i.e.*, with the tensile stress parallel to the preferential alignment of ceramic platelets (Fig. 2(b)). This is markedly higher than the flexural strength of the monolithic AZ91D Mg-alloy, which was measured to be 251 ± 13 MPa, and that of the Ti_3AlC_2 ceramic which is typically 330–550 MPa (although it has been reported that this can be enhanced with specific designs of micro- and nano-structures [36,37]). The fracture surface after bending displays obvious roughness at micro- to nano-scale levels. Such features, which confirm the material's architecture at characteristic dimensions, are caused by the much easier failure of the relatively weak metal phase and the pull-out of the ceramic platelets from the fracture surfaces, as illustrated in the inset in Fig. 2(b).

As shown in Fig. 3(a), the cermet material exhibits apparent hysteresis loops on the stress–strain curves under cyclic loading–unloading conditions at room temperature. This indicates the material's ability for dissipating mechanical energy from applied load by internal friction [4,38,39]. The dissipated energy at each loading–unloading cycle $E_{dissipated}$, as expressed by the area of hysteresis loop (inset in Fig. 3(b)), increases monotonically as the unloading stress increases. The ratio of $E_{dissipated}$ to the elastically restored energy $E_{elastic}$, *i.e.*, $E_{dissipated}/E_{elastic}$, for both the horizontal and vertical directions also demonstrates an increasing trend up to a value of ~0.4, provided the unloading stress exceeds 150 MPa. With respect to anisotropy, the $E_{dissipated}/E_{elastic}$ ratio is consistently higher along the vertical direction than along the horizontal direction for unloading stresses over 250 MPa.

Dynamic mechanical analysis (DMA) revealed that the cermet material shows superior internal friction Q^{-1} than the AZ91D Mg-alloy for all temperatures from ambient to 350 °C at a frequency of 1 Hz and strain amplitude of 1×10^{-4} (Fig. 3(c)). As the temperature is increased though, the Q^{-1} value of the cermet material increases more rapidly than that of the AZ91D Mg-alloy. At increasing strain amplitude from 1.7×10^{-5} to 4.3×10^{-4} at room temperature, the Q^{-1} of the cermet material becomes comparable to, or even higher than, that of the AZ91D Mg-alloy, and

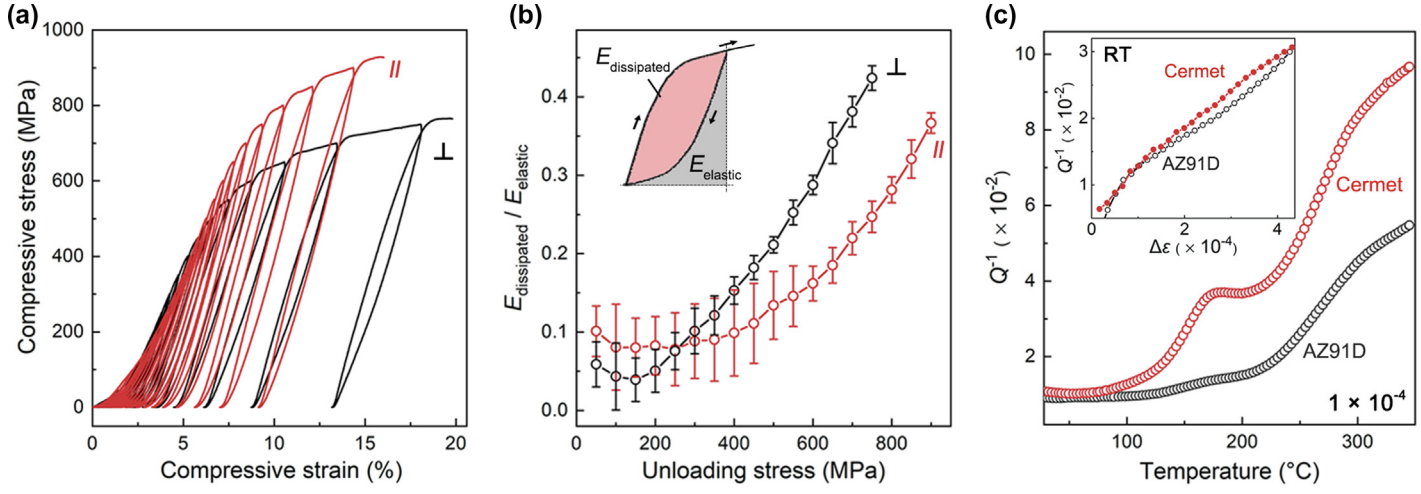

FIGURE 3

Energy dissipation and damping properties of the cermet material. (a) Cyclic compressive stress–strain curves of the cermet material loaded along the horizontal (∥) and vertical (⊥) directions at room temperature. (b) Variations in the ratio of dissipated energy, $E_{dissipated}$, to the elastically restored energy, $E_{elastic}$, as a function of the unloading stress for the horizontal and vertical directions of the cermet material. The inset illustrates the hysteresis loop and characteristic energies at each loading–unloading cycle. (c) Variations in the internal friction, Q^{-1}, which can be described as $E_{dissipated}/2\pi E_{stored}$ with $E_{dissipated}$ and E_{stored} denoting respectively the dissipated energy and the maximum stored energy during the cyclic loading for DMA measurement [38,39], as a function of the test temperature for the cermet material and AZ91D Mg-alloy at a constant strain amplitude of 1×10^{-4}. The inset shows the variations in Q^{-1} with increasing strain amplitude, $\Delta\varepsilon$, from 1.7×10^{-5} to 4.3×10^{-4} at room temperature (RT).

can be further increased with an increase in strain amplitude (inset in Fig. 3(c)). As such, the damping capacities of the cermet remain unchanged, or can even be further improved, as compared to AZ91D Mg-alloy despite the notable enhancement in its strength. Additionally, the cermet exhibits a reasonably sound fracture toughness of 16.4 ± 1.5 MPa $m^{1/2}$, although it is still prone to catastrophic fracture when tested in notched bending (Fig. S7). However, this toughness is comparable to that of magnesium and magnesium alloys, which generally ranges from ~5 to 33 MPa $m^{1/2}$, and significantly exceeds that of the Ti_3AlC_2 ceramic (typically of ~3.3–9.1 MPa $m^{1/2}$) [23,32,40]. As these K_{Ic} toughness values are primarily a function of the resistance to crack initiation, stable crack extension does not occur in the material, as is evident by the absence of any rising crack-resistance curve behavior.

Discussion

Materials may exhibit different strengths under different loading conditions. Specifically, uniaxial compression features a more confined stress state than bending with a larger ratio between the maximum values of shear stress to principal stress [41]. Nevertheless, the flexural strength is determined by the maximum tensile stress at the section with the highest bending moment, to some extent like in uniaxial tension. As such, bulk materials usually exhibit inferior strengths under bending than under compression – this is particularly pertinent for brittle materials which are more sensitive to defects [5,42]. Fig. 4(a) shows a comparison of the flexural strength versus compressive strength for magnesium (and magnesium alloys), ceramics, and the composite materials composed of them [10,14–16,18–20,32,40]. The flexural strengths are only comparable to the compressive strengths for materials with relatively low strengths where the compressive strength does not exceed 600 MPa. These materials mainly include monolithic magnesium and magnesium alloys and their composites reinforced by ceramics. However, the flexural strengths tend to be lower than the compressive strengths for relatively strong materials with compressive strength over 600 MPa, even by up to one order of magnitude for some ceramics. The current cermet material exhibits a comparatively high strength in excess of 1 GPa under both compressive and bending conditions, when the stress is parallel to the preferential alignment of ceramic platelets. Its flexural strength markedly surpasses that of its constituents, which is typically ~80 to 550 MPa for magnesium and magnesium alloys and 330–550 MPa for the Ti_3AlC_2 ceramic; it is also superior to the majority of other materials based on the magnesium-ceramic system.

The high flexural strength combined with a low density of 2.79 g cm^{-3}, which is comparable to that of aluminum alloys,

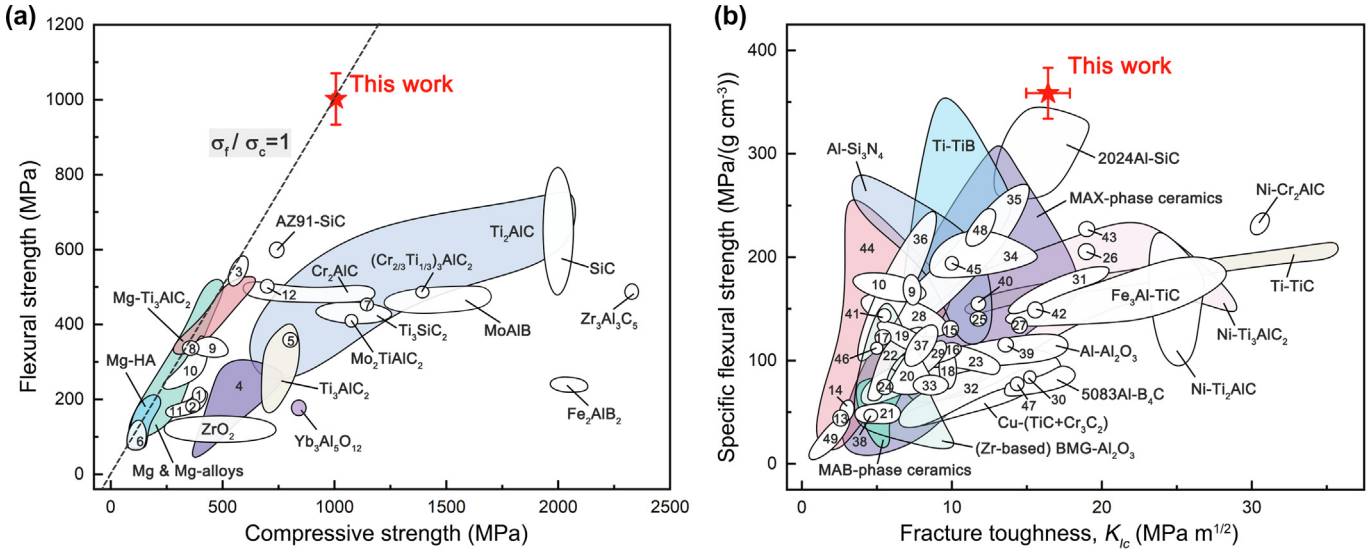

1.Al_2O_3	8.AZ91D-(CNT+Ti_3AlC_2)	15.NiAl-TiC	22.TiAl-Ti_2AlC	29.6061Al-Al_2O_3	36.TiAl-Al_2O_3	43.$Fe_{84}Al_{16}$-ZrO_2
2.AZ91D-Ti_3AlC_2	9.AZ91D-$Mg_2B_2O_{5W}$	16.(Ni3(Al,Ti)+NiAl)-TiC	23.Cu-Ti_3AlC_2	30.Ti-(ZrB_2+SiC)	37.Al-SiC	44.Structural ceramics
3.AZ91-Ti_3AlC_2	10.Mg-SiC	17.MgSi-B_4C	24.Zr_2Cu-ZrB_2	31.$Fe_{84}Al_{16}$-TiC	38.Cu-Al_2O_3	45.(Al-Si-Ti) alloy-Al_2O_3
4.V_2AlC	11.AZ61-Si	18.Ti-Al_2O_3	25.Fe_3Al-Al_2O_3	32.Cu-TiC	39.Al-TiC	46.Ni_2AlTi-TiC
5.Ta_2AlC	12.Ti_3AlC_2-(TiC+Al_2O_3)	19.(Al-Si) alloy-Al_2O_3	26.Fe_3Al-ZrO_2	33.Al-(Al_2O_3+ZrO_2)	40.$Fe_{84}Al_{16}$-Al_2O_3	47.Cu-(C/C+TiC)
6.Mg-B_4C	13.Ti_3AlC	20.6061Al-TiO_2	27.6061Al-TiC	34.2024Al-B_4C	41.$TiAl_3$-Ti_3AlC_2	48.2024Al-(B_4C+TiB_2)
7.$Mo_2Ti_2AlC_3$	14.Ni-Al_2O_3	21.Cu-(Ti_3SiC_2+TiC+SiC)	28.Ti-B_4C	35.ZL205A-SiC	42.ZL107-TiC	49.Zn-5Al alloy-(ZrB_2+SiC)

FIGURE 4

Comparison of mechanical properties for the cermet material with other materials. (a) Flexural strength versus compressive strength for ceramics, magnesium (and magnesium alloys), and the composite materials composed of them [10,14–16,18–20,32,40]. (b) Specific flexural strength, *i.e.*, flexural strength normalized by density, versus fracture toughness for ceramics and the cermet materials composed of ceramics and different types of metals other than magnesium [10,15,19–21,32,40,43–45]. CNT: carbon nanotube; $Mg_2B_2O_5$w: magnesium borate whisker; HA: hydroxyapatite; BMG: bulk metallic glass; MAB: ternary nano-laminated borides..

endows the cermet material with an outstanding specific flexural strength of 358 ± 24 MPa/(g cm^{-3}). As shown in Fig. 4(b), such a high specific flexural strength surpasses that of magnesium and most other magnesium alloys, ceramics, and cermet materials composed of ceramics and different types of metals other than magnesium [10,15,19–21,32,40,43–45]. With respect to toughness, it is difficult to realize both high specific flexural strength and good fracture toughness simultaneously in the above material systems. Specifically, their fracture toughness rarely exceeds 10 MPa $m^{1/2}$ once their specific flexural strength reaches 300 MPa/(g cm^{-3}) (exceptions have only been realized in Ti-TiB and 2024 Al alloy-SiC systems) [10,15,19–21,32,40,43–45]. In contrast, the current cermet material exhibits a reasonably good fracture toughness of 16.4 ± 1.5 MPa $m^{1/2}$ in addition to its high specific flexural strength and good damping capacity.

The high strength of the cermet material is closely related to its ultrafine 3D interpenetrated architecture. First, in line with the well-known Hall-Petch relationship [46], the metal phase is markedly strengthened by its ultrafine-grained structure, which is formed because of the constrained crystal growth within the narrow interspaces between ceramic platelets. Second, the number of relatively weak inter-layer bonds and in particular the large defects in the Ti_3AlC_2 ceramic can be largely reduced by ball milling the ceramic to ultrafine platelets. The micro-defects in the platelets introduced by ball milling can also be diminished during melt infiltration (Fig. S3). Third, the Ti_3AlC_2 phase develops strong interfacial bonding with magnesium and additionally exhibits a good wettability with the magnesium melt, which serves to minimize the formation of pores during infiltration (Fig. S2) [14,27]. The bi-continuous 3D interpenetrated architecture has also been shown to be beneficial for promoting an effective stress transfer in materials [4,35,47–49]. The obvious strength reduction of the cermet material at 200 °C and 350 °C is mainly caused by the creep behavior of the metal phase because of easy dislocation motion and grain boundary sliding [50,51], as shown in Fig. S6. Nevertheless, the strengths of the cermet at elevated temperatures still surpass those of most other magnesium alloys and their matrix composites [4,14,35,51,52].

Compared to monolithic ceramics and other cermet materials, the attainment of high strength in bending and under compression in the current cermet material can mainly be attributed to its lower sensitivity to defects resulting from its higher fracture toughness. The alternate arrangement of stiff (ceramic) and soft (metal) phases in a layered fashion, which is similar to the structural design of natural nacre, has been proved to be effective in toughening materials [1,2,28,29], *e.g.*, by deviating the cracks from straight propagation paths and bridging the crack faces to inhibit crack opening (inset in Fig. 2(b)). The good damping capacities of the cermet material are principally associated with the types of its components considering that both magnesium and Ti_3AlC_2 phase exhibit superior damping behavior respectively among metallic and ceramic systems [23,27]. The cermet's 3D interpenetrated structure is also critical as such architectures in composite materials have been revealed to be beneficial for retaining good damping characteristics [4,47].

Additionally, the ultrafine dimensions of both the metal and ceramic phases in the cermet provide abundant interfaces between them. Specifically, by assuming each platelet as a disk with a ~1 μm diameter and ~150 nm thickness, the number of platelets per unit volume (of 1 mm^3) in the cermet can be calculated to be ~3.7×10^9 considering the measured volume fraction of ceramic phase (~44.2 vol.%). The density of metal/ceramic interfaces can be roughly estimated using the surface area of platelets as ~7.5×10^3 mm^{-1} by ignoring the interconnections between them. Indeed, provided that the pores within the ceramic scaffold are fully infiltrated by the metal phase (Fig. S2), the density of metal/ceramic interfaces in the infiltrated composite can also be approximated using the specific surface area (*i.e.*, internal surface area per unit volume) of the scaffold before infiltration which was measured to be ~2.3×10^4 mm^{-1} using the mercury porosimetry method. This was of a similar order but somewhat higher than the calculated value, possibly because of the irregular shapes and rough surfaces of the ceramic platelets. A high fraction of interfaces has been well recognized to promote internal friction during vibration through a mechanism of enhanced dislocation nucleation at such interfaces due to the elastic and thermal mismatch between the constituents [38].

It is known that 3D interpenetrating-phase composites can be fabricated in different material systems (ceramic/polymer, ceramic/metal, metal/polymer, and metal/metal) by infiltrating the relatively soft phase into the porous scaffolds of hard phase [4,27,48,49,53–55]. In particular, the architectures can be constructed down to submicrometer- or even nano-scale dimensions, *e.g.*, in case of scaffolds made by interference lithography or 3D printing [48,49]. The micropillars of these composites (with diameter smaller than 10 μm) exhibit a high strength along with large plasticity under compression. Nevertheless, it is known that the mechanical properties of materials tend to show apparent improvement as the sample size decreases to such small dimensions [56,57]. By comparison, the current cermet material in its bulk form exhibits a high strength in excess of 1 GPa under both compressive and bending conditions, which markedly surpasses those of its counterparts in similar systems. Moreover, the current fabrication approach, by infiltrating the alloy melt into partially sintered ceramic scaffolds, is effective in constructing ultrafine 3D interpenetrated architectures in bulk cermet materials. The ceramic and metal contents in the cermet material, which were not modified in this study, can also be regulated during processing, for example, by adjusting the porosity of the ceramic scaffolds before infiltration via control of the sintering parameters.

Conclusions

In summary, a lightweight, strong, and damping cermet material comprising an ultrafine-grained AZ91D Mg-alloy and Ti_3AlC_2 ultrafine platelets was fabricated by infiltrating the alloy melt into a partially sintered ceramic scaffold. The metal and ceramic phases are bi-continuous and interpenetrated in 3D space in the cermet material, and are alternately arranged in a layered fashion as in natural nacre. The cermet material exhibits high strength in excess of 1 GPa under both compressive and bending conditions at room temperature, with a high specific flexural strength of 358 ± 24 MPa/(g cm^{-3}). In fact, its flexural strength and specific flexural strength surpass those of most other magnesium and magnesium alloys, ceramics and cermet materials. This is accom-

panied by improved strength at elevated temperatures, reasonably good fracture toughness, and enhanced damping capacities at ambient to elevated temperatures, as compared to the AZ91D Mg-alloy. Such a sound combination of properties makes this cermet an appealing candidate material for many structural applications, such as load-bearing applications where lightweight materials are required and for reducing vibrations at high stress levels. Additionally, the design strategy of the architecture utilized here, which encompasses the ultrafine dimensions of constituents combined with the nacre-like arrangement of metal and ceramic phases and their interpenetration in 3D space, may afford insights for the development of new high-performance cermet materials.

Methods

Materials preparation

Ti_3AlC_2 MAX phase was synthesized by sintering the mixed powders of TiAl (99.5 wt.%, ~300 mesh) and TiC (99 wt.%, 2–4 μm) with a molar ratio of 1:1.9 *in vacuo* at 1500 °C under a pressure of 30 MPa for 2 h. The sintered bulk was crushed to coarse powders, and then were ball milled in an ethanol dispersant in a mixed gas of 20 vol.% oxygen and 80 vol.% argon at a speed of 500 rpm for 48 h, followed by drying in air for 2 days. The MAX phase was delaminated into ultrafine platelets during ball milling due to the relatively weak inter-layer bonding of the layered structure, as shown in Fig. S8. The equivalent particle size of the resulting Ti_3AlC_2 platelets was measured using laser diffraction granulometry to be mostly in the range of 100 to 300 nm. The oxygen contents of the MAX phase before and after ball milling were measured using a TCH-600 N/H/O analyzer (LECO, USA).

The Ti_3AlC_2 platelets were dispersed into ethanol at a mass ratio of 3:40 by ultrasonic treatment at 50 W for 0.5 h and then ball milled at a speed of 25 rpm for 24 h. The suspension was poured into a funnel of 55 mm in diameter and filtrated through a nylon membrane filter with pore size of 0.1 μm under a vacuum of ~0.06 MPa. The platelets were driven to deposit on the membrane and be preferentially aligned along the horizontal direction during this process. The deposited bulk was dried and pressed along the vertical direction at 72 MPa for 1 h, and then partially sintered in flowing argon gas at 900 °C for 1 h to form interconnections between adjacent platelets. This produced an open porous scaffold of the Ti_3AlC_2 phase where the pores and ceramic platelets were preferentially aligned and interpenetrated in 3D space (Fig. S1). The porosity and specific surface area of the scaffolds were measured using the mercury porosimetry method with an AutoPore IV 9500 porosimeter (Micromeritics, USA). The Ti_3AlC_2 scaffold was then infiltrated with a melt of commercial AZ91D Mg-Al-Zn alloy (Mg with ~8.5–9.5 wt.% Al, ~0.45–0.9 wt.% Zn and ~0.17–0.5 wt.% Mn) in flowing argon gas at 850 °C, *i.e.*, ~250 °C higher than the melting point of the alloy, for 1.5 h using a SRYL-2300/9 graphite resistance furnace (Jvjing Instrument, China), and then cooled with the furnace. The original AZ91D Mg-alloy was in an as-cast state and had a grain size of 50–150 μm.

Microstructure and phase analysis

The density of the infiltrated cermet material was measured using the Archimedes' method. The phase constitution was determined by X-ray diffraction (XRD) using a Bruker D8 Advance diffractometer (Bruker AXS, Germany) with Cu-Kα radiation. Scanning electron microscopy (SEM) imaging was conducted using an Inspect F50 field-emission scanning electron microscope (FEI, USA) at an accelerating voltage of 20 kV. Transmission electron microscopy (TEM) and scanning TEM imaging was performed using a Tacnai-G2 F30 transmission electron microscope (FEI, USA) at an accelerating voltage of 300 kV. The TEM samples were prepared by cutting thin slices from the cermet material through its thickness, *i.e.*, along the vertical direction. The slices were manually ground and polished to a thickness of ~30 μm, dimpled to a thickness of ~15 μm, and then ion milled using a Gatan 695 precision ion polishing system (Gatan, USA). The TEM images were analyzed using the Image-Pro Plus software (Media Cybernetics, USA). The element distribution was characterized by energy-dispersive X-ray spectroscopy (EDS) using the microscope. X-ray tomography (XRT) imaging was performed using an Xradia Versa XRM-500 3D X-ray microscope (Xradia, USA) operating at an accelerating voltage of 80 kV. A total of 1600 slices of 2D projections were acquired for the XRT imaging, and then were reconstructed to 3D volume renderings based on the Fourier back-projection algorithm. The spatial resolution of the obtained XRT images was ~0.89 μm per pixel.

Mechanical testing

Uniaxial compression tests were performed at room temperature, 200 °C and 350 °C using an Instron 5982 testing system (Instron, USA) with a constant strain rate of 10^{-3} s^{-1} on cuboid samples with dimensions of 2 mm × 2 mm × 4 mm. The compressive loads were applied along the horizontal and vertical directions of the cermet material, *i.e.*, respectively parallel and perpendicular to the preferential alignment of the ceramic platelets. The ceramic scaffold before infiltration and AZ91D Mg-alloy were also tested for comparison. Additionally, the samples of the cermet material were repeatedly loaded and unloaded at room temperature with a constant stress increase of 50 MPa at each cycle until fracture. The compressive deformation of samples at room temperature was measured using an Instron 2601–92 linear variable differential transformer position sensor. Three-point bending tests were performed using an Instron E1000 testing system (Instron, USA) at room temperature with a constant displacement rate of 0.1 mm/min on beam samples with dimensions of 2 mm × 1.5 mm × 25 mm and a loading span of 20 mm, in line with the ASTM Standard C1161 [58]. The loads were applied along the vertical direction, *i.e.*, perpendicular to the preferential alignment of ceramic platelets in the cermet material, which is consistent with the general loading configuration for natural nacre.

Single-edge notched three-point bending tests were performed on a JEOL MicroTest stage inside the chamber of a JEOL JSM-6510 scanning electron microscope (JEOL, Japan) at a displacement rate of 0.005 mm/min using beam samples with a width of 4 mm, thickness of 2 mm and loading span of 16 mm. The loading direction was also perpendicular to the preferential alignment of the ceramic platelets. The side notch was cut to ~2 mm in depth using a low-speed diamond wire saw, and then sharpened to a tip radius of 5–10 μm using a razor blade

with 1 μm diamond paste. The testing methods and sample dimensions were generally in accordance with the ASTM Standard E1820 [59]. The fracture morphologies of samples were characterized by SEM imaging.

Thermal and dynamic mechanical analysis

Thermogravimetry (TG) and differential thermal analysis (DTA) experiments were performed by heating samples at 10 °C/min to 600 °C in flowing air with a flow rate of 50 mL/min using a STA 449F5 thermal analyzer (NETZSCH, Germany). The room-temperature damping capacities of the cermet material and the AZ91D Mg-alloy were measured by dynamic mechanical analysis (DMA) under a single cantilever bending mode on beam samples with dimensions of 3 mm × 2 mm × 35 mm using a DMA Q800 dynamic mechanical analyzer (TA Instrument, USA). The measurement was conducted at a frequency of 1 Hz with the strain amplitude ranging from 1.7×10^{-5} to 4.3×10^{-4}. The applied load was perpendicular to the preferential alignment of ceramic platelets for the cermet material. The damping capacities at elevated temperatures up to 350 °C were also measured at a constant strain amplitude of 1×10^{-4} and a frequency of 1 Hz with the same loading configuration.

Data availability

Data will be made available on request.

Declaration of Competing Interest

The authors declare that they have no known competing financial interests or personal relationships that could have appeared to influence the work reported in this paper.

Acknowledgments

The authors are grateful for the financial support by the National Key R&D Program of China (2020YFA0710404), the National Natural Science Foundation of China (52173269 and 51871216), the KC Wong Education Foundation (GJTD-2020-09), and the Youth Innovation Promotion Association CAS (2019191). ROR acknowledges the support from the Multidisciplinary University Research Initiative to University of California Riverside, funded by the Air Force Office of Scientific Research (AFOSR-FA9550-15-1-0009) and subcontracted to the University of California Berkeley.

Appendix A. Supplementary material

Supplementary data to this article can be found online at https://doi.org/10.1016/j.mattod.2022.12.002.

References

[1] R.O. Ritchie, Nat. Mater. 10 (2011) 817–822, https://doi.org/10.1038/nmat3115.
[2] B.J. Zhang et al., Mater. Today 41 (2020) 177–199, https://doi.org/10.1016/j.mattod.2020.04.009.
[3] Z.F. Lei et al., Sci. Adv. 6 (2020) eaba7802, https://doi.org/10.1126/sciadv.aba7802.
[4] M.Y. Zhang et al., Sci. Adv. 6 (2020) eaba5581, https://doi.org/10.1126/sciadv.aba5581.
[5] S. Ban, K.J. Anusavice, J. Dent. Res. 69 (1990) 1791–1799, https://doi.org/10.1177/00220345900690120201.
[6] D.M. Roy, Science 235 (1987) 651–658, https://doi.org/10.1126/science.235.4789.651.
[7] T.M. Pollock, Science 328 (2010) 986–987, https://doi.org/10.1126/science.1182848.
[8] W.Q. Xu et al., Nat. Mater. 14 (2015) 1229–1235, https://doi.org/10.1038/nmat4435.
[9] M. Caccia et al., Nature 562 (2018) 406–409, https://doi.org/10.1038/s41586-018-0593-1.
[10] J.S. Moya, S. Lopez-Esteban, C. Pecharroman, Prog. Mater. Sci. 52 (2007) 1017–1090, https://doi.org/10.1016/j.pmatsci.2006.09.003.
[11] L.Y. Chen et al., Nature 528 (2015) 539–543, https://doi.org/10.1038/nature16445.
[12] W.H. Yu et al., Prog. Mater. Sci. 104 (2019) 330–379, https://doi.org/10.1016/j.pmatsci.2019.04.006.
[13] T. Klunsner et al., Acta Mater. 188 (2020) 30–39, https://doi.org/10.1016/j.actamat.2020.01.057.
[14] L. Rangaraj et al., Metall. Mater. Trans. A 50 (2019) 3714–3723, https://doi.org/10.1007/s11661-019-05289-8.
[15] H. Zhang et al., Mater. Lett. 183 (2016) 299–302, https://doi.org/10.1016/j.matlet.2016.07.126.
[16] G.G. Xiong et al., Curr. Appl. Phys. 16 (2016) 830–836, https://doi.org/10.1016/j.cap.2016.05.004.
[17] D.J. Lloyd, Int. Mater. Rev. 39 (1994) 1–23, https://doi.org/10.1179/imr.1994.39.1.1.
[18] F. Zeng et al., J. Alloys Compd. 728 (2017) 413–423, https://doi.org/10.1016/j.jallcom.2017.09.043.
[19] H.R. Mao et al., J. Mater. Sci. 53 (2018) 12167–12177, https://doi.org/10.1007/s10853-018-2491-1.
[20] J. Schroder, Mater. Sci. Eng. A 135 (1991) 33–36, https://doi.org/10.1016/0921-5093(91)90532-R.
[21] X. Luo et al., J. Alloys Compd. 855 (2021), https://doi.org/10.1016/j.jallcom.2020.157359 157359.
[22] M. Cafri et al., J. Eur. Ceram. Soc. 32 (2012) 3477–3483, https://doi.org/10.1016/j.jeurceramsoc.2012.04.007.
[23] Z.M. Sun, Int. Mater. Rev. 56 (2011) 143–166, https://doi.org/10.1179/1743280410Y.0000000001.
[24] M.A. Tunes et al., Sci. Adv. 7 (2021) eabf6771, https://doi.org/10.1126/sciadv.abf6771.
[25] C.J. Gilbert et al., Scr. Mater. 42 (2000) 761–767, https://doi.org/10.1016/S1359-6462(99)00427-3.
[26] D. Chen et al., J. Am. Ceram. Soc. 84 (2001) 2914–2920, https://doi.org/10.1111/j.1151-2916.2001.tb01115.x.
[27] B. Anasori, E.N. Michel, M.W. Barsoum, Mater. Sci. Eng. A 618 (2014) 511–522, https://doi.org/10.1016/j.msea.2014.09.039.
[28] G. Mayer, Science 310 (2005) 1144–1147, https://doi.org/10.1126/science.1116994.
[29] M. Grossman et al., Adv. Mater. 29 (2017) 1605039, https://doi.org/10.1002/adma.201605039.
[30] A. Amini et al., Science 373 (2021) 1229–1234, https://doi.org/10.1126/science.abf0277.
[31] H.J. Rathod et al., Sci. Adv. 7 (2021) eabg2549, https://doi.org/10.1126/sciadv.abg2549.
[32] X. Xie et al., J. Mater. Sci. Technol. 38 (2020) 86–92, https://doi.org/10.1016/j.jmst.2019.05.070.
[33] L.R. Meza, S. Das, J.R. Greer, Science 345 (2014) 1322–1326, https://doi.org/10.1126/science.1255908.
[34] M.K. Habibi, S.P. Joshi, M. Gupta, Acta Mater. 58 (2010) 6104–6114, https://doi.org/10.1016/j.actamat.2010.07.028.
[35] M.Y. Zhang et al., Compos. Part B Eng. 215 (2021), https://doi.org/10.1016/j.compositesb.2021.108783 108783.
[36] M.W. Barsoum, M. Radovic, Annu. Rev. Mater. Res. 41 (2011) 195–277, https://doi.org/10.1146/annurev-matsci-062910-100448.
[37] Y.C. Zhou, J.X. Chen, J.Y. Wang, Acta Mater. 54 (2006) 1317–1322, https://doi.org/10.1016/j.actamat.2005.10.057.
[38] J. Zhang, R.J. Perez, E.J. Lavernia, J. Mater. Sci. 28 (1993) 2395–2404, https://doi.org/10.1007/BF01151671.
[39] H. Soul et al., Smart Mater. Struct. 19 (2010), https://doi.org/10.1088/0964-1726/19/8/085006 085006.
[40] X.H. Wang, Y.C. Zhou, Acta Mater. 50 (2002) 3143–3151, https://doi.org/10.1016/S1359-6454(02)00117-9.
[41] J.M. Ramsey, F.M. Chester, Nature 428 (2004) 63–66, https://doi.org/10.1038/nature02333.
[42] Y.C. Wang et al., Nat. Mater. 20 (2021) 1371–1377, https://doi.org/10.1038/s41563-021-01017-z.

[43] Y.C. Jin et al., Ceram. Int. 47 (2021) 2766–2771, https://doi.org/10.1016/j.ceramint.2020.09.130.
[44] A. Wat et al., Nat. Commun. 10 (2019) 961, https://doi.org/10.1038/s41467-019-08753-6.
[45] Z.J. Hu et al., Scr. Mater. 186 (2020) 312–316, https://doi.org/10.1016/j.scriptamat.2020.05.029.
[46] C.S. Pande, K.P. Cooper, Prog. Mater. Sci. 54 (2009) 689–706, https://doi.org/10.1016/j.pmatsci.2009.03.008.
[47] L.F. Wang et al., Adv. Mater. 23 (2011) 1524–1529, https://doi.org/10.1002/adma.201003956.
[48] J.H. Lee et al., Nano Lett. 12 (2012) 4392–4396, https://doi.org/10.1021/nl302234f.
[49] J. Bauer et al., Sci. Adv. 8 (2022) eabo3080, https://doi.org/10.1126/sciadv.abo3080.
[50] H. Hu et al., Mater. Manuf. Process. 18 (2003) 687–717, https://doi.org/10.1081/AMP-120024970.
[51] A. Srinivasan et al., Mater. Sci. Eng. A 527 (2010) 1395–1403, https://doi.org/10.1016/j.msea.2009.10.008.
[52] A.A. Luo, Int. Mater. Rev. 49 (2004) 13–30, https://doi.org/10.1179/095066004225010497.
[53] X. Chen et al., Mater. Des. 215 (2022), https://doi.org/10.1016/j.matdes.2022.110531 110531.
[54] M.Y. Zhang et al., Appl. Mater. Today 29 (2022), https://doi.org/10.1016/j.apmt.2022.101639 101639.
[55] M. Zhang et al., Nat. Commun. 13 (2022) 3247. https://www.nature.com/articles/s41467-022-30873-9.
[56] M.D. Uchic et al., Science 305 (2004) 986–989, https://doi.org/10.1126/science.1098993.
[57] J.R. Greer, W.C. Oliver, W.D. Nix, Acta Mater. 53 (2005) 1821–1830, https://doi.org/10.1016/j.actamat.2004.12.031.
[58] , American Society for Testing and Materials International, West Conshohocken, PA, USA, 2018.
[59] , American Society for Testing and Materials International, West Conshohocken, PA, USA, 2013.